

In situ observation of cluster formation during nanoparticle solution casting on a colloidal film

This article has been downloaded from IOPscience. Please scroll down to see the full text article.

2011 J. Phys.: Condens. Matter 23 254208

(<http://iopscience.iop.org/0953-8984/23/25/254208>)

View [the table of contents for this issue](#), or go to the [journal homepage](#) for more

Download details:

IP Address: 130.209.6.41

The article was downloaded on 05/04/2012 at 15:48

Please note that [terms and conditions apply](#).

In situ observation of cluster formation during nanoparticle solution casting on a colloidal film

S V Roth¹, G Herzog^{1,2}, V Körstgens³, A Buffet¹, M Schwartzkopf¹, J Perlich¹, M M Abul Kashem¹, R Döhrmann¹, R Gehrke¹, A Rothkirch¹, K Stassig¹, W Wurth², G Benecke^{1,4}, C Li⁴, P Fratzl⁴, M Rawolle³ and P Müller-Buschbaum³

¹ Deutsches Elektronen-Synchrotron (DESY), Notkestraße 85, D-22607 Hamburg, Germany

² Institut für Experimentalphysik, Luruper Chaussee 149, D-22761 Hamburg, Germany

³ TU München, Physik Department, Lehrstuhl für Funkt. Mat., James-Franck-Straße 1, D-85748 Garching, Germany

⁴ MPI für Colloids and Interfaces Golm, Abteilung Biomat., Wissenschaftspark Potsdam-Golm, D-14424 Potsdam, Germany

E-mail: stephan.roth@desy.de

Received 14 January 2011, in final form 1 March 2011

Published 8 June 2011

Online at stacks.iop.org/JPhysCM/23/254208

Abstract

We present a real-time study of the nanostructuring and cluster formation of gold nanoparticles deposited in aqueous solution on top of a pre-structured polystyrene colloidal thin film. Cluster formation takes place at different length scales, from the agglomerations of the gold nanoparticles to domains of polystyrene colloids. By combining *in situ* imaging ellipsometry and microbeam grazing incidence small-angle x-ray scattering, we are able to identify different stages of nanocomposite formation, namely diffusion, roughness increase, layer build-up and compaction. The findings can serve as a guideline for nanocomposite tailoring by solution casting.

(Some figures in this article are in colour only in the electronic version)

1. Introduction

Nanoparticle metal–polymer composite thin films have become widely used in modern technologies and functional applications [1]. Prominent examples are catalysis [2], magnetic data storage [3–5], optical technology [6–14], memory devices [15, 16], coatings [17], sensors [18, 19] and biomimetic applications [20, 21]. Among wet casting methods to produce colloidal thin films, inkjet printing [22] and solution casting is widely applied [23, 24]. The latter allows for installing designed colloidal, polymeric and biopolymeric thin films [25–27]. The advantage is that tailored morphologies and gradients for combinatorial investigations of thin films [23, 27] are rapidly installed. Arrays of ordered colloidal and nanoparticles are very interesting for high-throughput applications such as surface enhanced Raman scattering (SERS) [28], colorimetric detection of biopolymers [29] or sensors [30, 31].

Recent developments include the use of nanoparticles in photovoltaic devices to install designed voids for an increase in light harvesting efficiency [32]. Here, different distinct particle sizes are incorporated into the polymeric matrix to obtain broadband light harvesting. This requires an understanding of the wetting and flow behaviour and thus the nanostructuring of colloidal thin films on top of nanostructured substrates. The use of distinct nanoparticle sizes on the substrate and in the cast solution is very appealing, as it permits the installation of regions of distinct structures on multiple length scales induced by solvent evaporation.

Colloidal solution casting and nanostructuring consists of complex non-equilibrium processes. The colloids self-assemble during the evaporation of the solvent involving the interplay of several flow- and time-dependent mechanisms. Rheology, phase changes and non-equilibrium thermodynamics [33, 34] play an important role. Nanostructuring takes place at the triple phase contact line, air–colloidal solution–

substrate [25]. This means that nanostructuring happens when the solution film is already thinned out [35]. In general, the rate of evaporation of the solvent varies along the droplet surface and is increased near the contact line. The colloidal nanoparticles are transported toward the outer rim of the droplet due to convective flow [36] or in the opposite direction, depending on the ratio of the surface tensions of solute and solvent [37]. Moreover, this instability is amplified by compositional [33] and temperature [38] driven Marangoni flows which pull the fluid towards the cooler rim. The contact line might become unstable [39] and capillary forces [40] also play a role. The installed structures typically show multiple length scales [41–43], varying from the individual nanoparticle size to μm or mm sized domains.

In this study, we focus on the nanostructuring of a gold (Au) colloidal solution being drop-cast on top of an ordered polystyrene (PS) colloidal layer. To obtain a deeper insight into the structure formation process, we combined *in situ* imaging ellipsometry and microbeam grazing incidence small-angle x-ray scattering (μGISAXS) [44] in a novel way. Thus, we performed an *in situ* experiment, monitoring the structural changes and layer build-up during the drop-casting process and subsequently scanned the Au–PS nanocomposite.

2. Experimental details

We used several *ex situ* and *in situ* methods to characterize the solution casting process, namely optical microscopy and atomic force microscopy as well as imaging ellipsometry and microbeam grazing incidence small-angle x-ray scattering. In this section, we briefly describe the different methods.

2.1. Materials and sample preparation

For cleaning purposes the silicon Si(100) substrate (SiMat Company, Germany) with a dimension of $75 \times 25 \text{ mm}^2$ was stored in dichloromethane at room temperature for 30 min, then put in deionized water at room temperature for 20 min and subsequently put in a basic bath consisting of 350 ml deionized water, 35 ml 25% ammonia solution and 25 ml 35% hydrogen peroxide at 65°C . This basic bath was then heated to 75°C for 120 min. Next, the Si substrate was rinsed with deionized water and dried with nitrogen. 150 μl of a 5% aqueous suspension of carboxylated PS colloids with a nominal diameter of 100 nm (Kisker) were spin-coated onto the substrate at 4000 rpm for 120 s. The sample was brought into an inclined position such that one end of the 75 mm long sample was elevated relative to its other end. The angle of inclination was 13° . A toluene drop of 20 μl was dropped onto the sample and it flowed along the long direction of the sample while drying. As a result, a channel of about 5 mm width and 60 mm length was formed, and with respect to the 25 mm direction it is in the centre of the sample.

For the colloidal droplet solution casting, we used uncoated gold (Au) nanoparticles in aqueous solution from Nanocs, Inc. The Au nanospheres have a nominal diameter of 20 nm. The droplet of $(33 \pm 8) \mu\text{l}$ was deposited on the sample surface using a remotely controlled standard syringe

pump (Harvard Apparatus). Prior to deposition, the colloidal solution was infused into the syringes using a micropipetting system. The relative humidity was $38 \pm 2\%$ and the ambient temperature $24 \pm 2^\circ\text{C}$.

2.2. Optical microscopy

An overview of the droplet was obtained by optical microscopy (OM). We employed a high resolution microscope system (VHX, Keyence). Figure 1(a) gives a composite image of the droplet deposition area after deposition. The different morphologies of the installed laterally heterogeneous PS film (see section 2.1) and the droplet position are visible. The beam position for the *in situ* experiment as well as the scanned area are marked.

2.3. Atomic force microscopy

Real space topographic images on the nanometric scale were acquired by atomic force microscopy (AFM, NT-MDT NTEGRA Aura System) in semi-contact mode. The results are shown in figure 2 and are correlated with the OM image in figure 1.

2.4. Ellipsometry

An imaging ellipsometer called a surface probe ellipsometric microscope (SPEM) (Nanofilm Technologie GmbH) was installed. Its purpose is on the one hand to locate and characterize an interesting spot on the sample with imaging ellipsometry. On the other hand it allows for running an *in situ* μGISAXS experiment during the evaporation process while monitoring the ellipsometric values Δ and Ψ [44]. The experimental ellipsometry data are expressed as relative amplitude ratio ($\tan(\Psi)$) and relative phase shift (Δ), related to the Fresnel reflection coefficients R_p and R_s for p- and s-polarized light, respectively. These coefficients are complex functions of the angle of incidence Φ_0 , the wavelength λ_{LASER} , the optical constants of the substrate (N_S), the ambient medium (n_0), and the layers (n_j, k_j, d_j) with n being the refractive index, k the extinction coefficient and d_j the layer thicknesses [45]:

$$\tan(\Psi) \exp(i\Delta) = \frac{R_p}{R_s} = F(\Phi_0, \lambda_{\text{LASER}}, N_S, n_0, n_j, k_j, d_j), \quad (1)$$

with $j = 0-2$, (number of layers). The imaging ellipsometer installed is a single wavelength (532 nm) nulling instrument in polarizer–compensator–sample–analyser (PCSA) configuration. The angle of incidence for the laser beam can be varied with a motorized goniometer between 42° and 80° . The sample was aligned with respect to the ellipsometer with a combination of a two-circle segment and an xyz stage. The imaging ellipsometer comprises a CCD camera and an objective with a motorized focusing mechanism for capturing images. Changing the settings of the polarizer, compensator and analyser allows us to meet the nulling condition for every region or pixel resolved with the detector. Due to the inclined

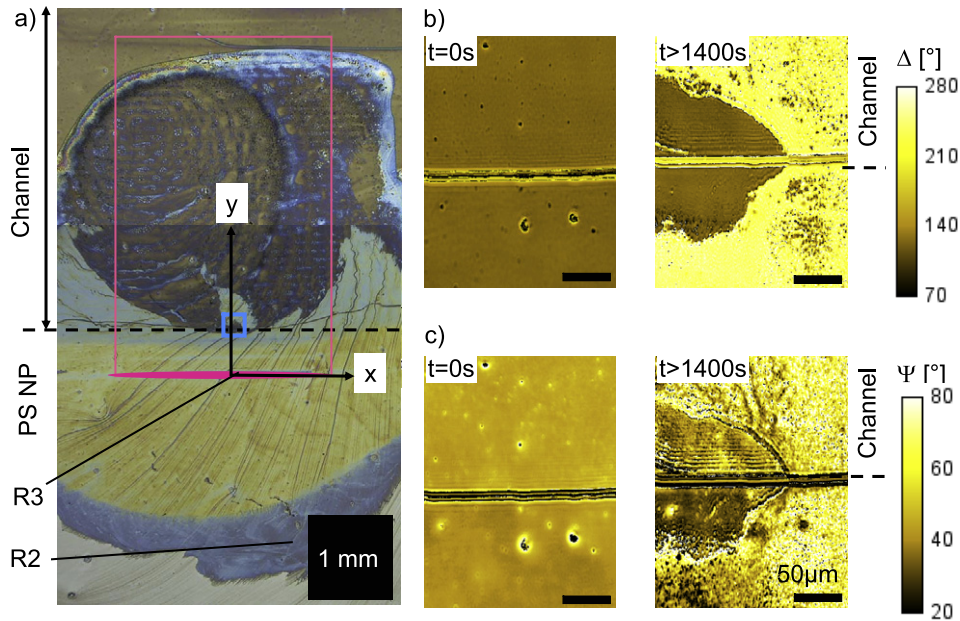


Figure 1. (a) Composite optical microscopy image. x denotes the x-ray beam direction. z is vertical to the x/y -plane. Indicated is the scale (1 mm) and the beam position for the *in situ* experiments. The pink rectangle shows the scanning area. On top, the channel created by the toluene treatment is visible. PS NP denotes the PS colloidal layer. R2 and R3 correspond to the position of the AFM images (see figure 2). (b) Δ map of the region indicated by the blue square in (a). $t = 0$ s denotes time prior to droplet deposition, $t > 1400$ s denotes the final dried state. (c) Corresponding Ψ map. The scale is indicated.

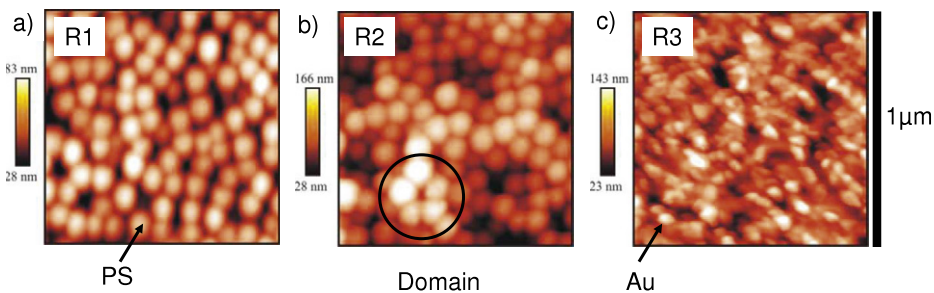


Figure 2. Atomic force microscopy (AFM) topography images. (a)–(c) AFM images of the pristine PS film (named R1), R2 and R3 correspond to the different regions of the droplet R2 and R3 in figure 1. ‘PS’ denotes the individual PS colloid, ‘domain’ indicates the area of clustered PS colloids and ‘Au’ the agglomeration of the individual Au nanoparticles.

observation angle in ellipsometry, in principle only a small region is in focus. With the SPEM imaging ellipsometer this is overcome by collecting a series of images with different foci within the field of view and a subsequent digital image processing system where these images are superimposed to give one overall-focused image. In this study an objective providing $20\times$ magnification was used yielding a lateral resolution of $1\ \mu\text{m}$. The area seen by the detector depends on the angle of incidence applied. For an angle of incidence of 55° for the laser beam, as used in this experiment, the field of view is about $201 \times 263\ \mu\text{m}^2$. In the field of view it is possible to assign regions of interest in which the ellipsometric values are averaged. For the *in situ* evaporation experiment a region of interest matching the footprint of the x-ray beam on the sample was used [44].

2.5. Microbeam grazing incidence small-angle x-ray scattering

Microbeam grazing incidence small-angle x-ray scattering (μGISAXS) is a powerful technique for *in situ* investigations of non-equilibrium and kinetic processes [25, 35]. Owing to the footprint due to the grazing incidence conditions, the results are of statistical relevance. Combined with a micro-focused beam, laterally heterogeneous multilayer thin films are accessible and can be investigated locally [46, 47, 34, 48].

In μGISAXS geometry, the incident beam impinges under a low angle (typically $\alpha_i \leq 1^\circ$) onto the sample surface [49, 50]. The beam is then specularly and diffusely scattered. A reciprocal space coordinate system is defined by the wavevector transfers perpendicular (parallel to z) and

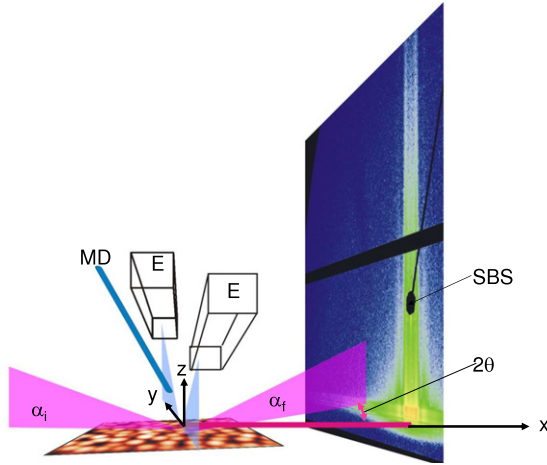


Figure 3. Geometry of the microbeam GISAXS experiment. α_i denotes the incident angle of the x-ray beam to the sample surface, α_f the exit angle and 2θ the out-of-plane angle. The incident plane is defined by x and z . y is perpendicular to this plane. E denotes the two ellipsometer arms (laser and detector), their detection plane (blue) being perpendicular to the incident plane of the x-ray beam. MD denotes the retractable micropipetting system for droplet deposition, SBS denotes the specular beam stop.

horizontal (parallel to y) with respect to the sample surface:

$$q_z = \frac{2\pi}{\lambda}(\sin(\alpha_i) + \sin(\alpha_f)) \quad (2)$$

and

$$q_y = \frac{2\pi}{\lambda} \sin(2\theta), \quad (3)$$

with λ being the wavelength of the incident x-ray beam and α_i and α_f the incident and exit angles, respectively. Thus correlations perpendicular and parallel to the sample surface can be deduced, for example layer correlations and lateral length scales (radii, mean distances etc). Typically, layer correlations show up as resonant diffuse scattering, i.e. oscillations and fringes of the intensity along q_z . A special feature to mention is the so-called Yoneda peak [51]. It arises as an interference effect between incoming and outgoing x-ray beam and occurs at the critical angle of the materials involved: $\alpha_{i,f} = \alpha_c = \sqrt{2\delta}$ with $1 - \delta$ being the real part of the complex index of refraction. In our case, the critical angle for silicon (Si) is $\alpha_c = 0.141^\circ$. The intensity is enhanced because the standing wave fields of the incident and reflected waves reached their maxima [49].

The μ GISAXS experiments were performed at the micro- and nanofocus x-ray scattering beamline (MiNaXS/P03) at the third generation synchrotron source PETRA III of the Deutsches Elektronen-Synchrotron (DESY) in Hamburg, Germany. In detail, we produced a micro-focused x-ray beam using a set of 12 beryllium compound refractive lenses (BeCRLs) [52] based at 81.762 m from the high-beta undulator source, leading to a beam size of $35 \times 22 \mu\text{m}^2$ ($H \times V$) at the sample position. To reduce crossfire, guard slits with an effective opening of $250 \mu\text{m}$ were used in front of the specimen. The energy used was 12.78 keV, monochromatized by a vertical large-offset double crystal

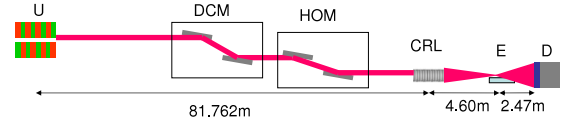


Figure 4. Sketch of the beamline layout for the combined imaging ellipsometry and μ GISAXS experiment. U denotes the undulator source, DCM the double crystal Si(111) fixed-exit monochromator, HOM the fixed-exit higher order suppression mirrors, CRL the set of $N = 12$ beryllium compound refractive lenses, E the sample position and D the detector. The sample-to-detector distance used was 2.470 m.

monochromator using Si(111) crystals. To suppress the higher harmonics from the undulator source, a pair of vertical deflection mirrors (molybdenum coating on quartz substrate) was incorporated. As a detector, we used a PILATUS 300k (Dectris, Switzerland), with 487×619 pixels ($H \times V$) and a pixel size of $172 \mu\text{m}$ in both horizontal and vertical directions. The sample-to-detector distance SDD was chosen as 2470 mm. The direct as well as the specularly reflected beam were masked by two separate point-like beam stops to avoid saturation of the detector. As the angle of incidence in μ GISAXS geometry, we chose $\alpha_i = 0.45^\circ$, greater than all critical angles of the materials involved. The overall layout and focusing distances of the MiNaXS beamline are shown in figure 4. In figure 3 a sketch of the combined μ GISAXS ellipsometry setup is shown. The imaging ellipsometer was mounted on a heavy-load Huber goniometer stage, allowing for full angular and translational control of the imaging ellipsometer in the micro-focused x-ray beam. The optical laser and the x-ray beam are perpendicular to each other. At the cross-over point, the colloidal solution was deposited using a motorized, remotely controlled micropipetting system. Most of the x-ray beam path was evacuated, with exception of the sample position, in order to be able to freely move the imaging ellipsometer.

The detailed basic principle of combined imaging ellipsometry with μ GISAXS is described in [44]. To align the sample in both the x-ray beam and the ellipsometer, a two-stage procedure is used. First the sample is placed on the xy plane (horizontal) of the translation stage of the ellipsometer and the ellipsometric alignment is performed. Then, α_i is set by tilting the whole ellipsometer setup (including the detector and laser arm) by an independent heavy-load two-circle segment, thus not affecting the sample's ellipsometric alignment and allowing for simultaneous independent *in situ* ellipsometric measurements in combination with μ GISAXS for all desired incident angles.

2.6. Data visualization and analysis

The data treatment consisted of a two step procedure. First, the data were visualized using the software package DPDAK [53]. Secondly quantitative analysis was performed using the software package IsGISAXS [54] to extract quantitative information.

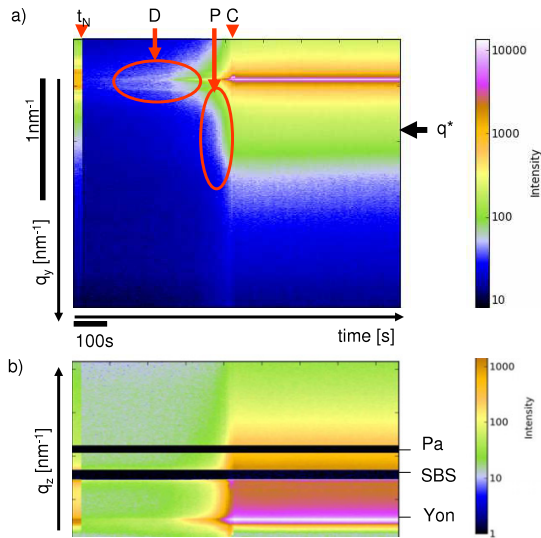


Figure 5. (a) Contour plot of the intensity of the out-of-plane cuts as a function of time (map of out-of-plane cuts at the critical angle α_c of Si). t_N denotes the time of droplet deposition, D the time region of rearrangement of the PS layer, P the precipitation and agglomeration of the Au nanoparticles and C the compaction of the rearranged and precipitated layers. q^* denotes the Au agglomerates. (b) Corresponding map of the detector cuts. q_y and q_z with their corresponding scale bar are indicated. Yon denotes the Yoneda peak position, SBS the position of the specular beam stop, Pa indicates empty pixels due to non-sensitive areas between adjacent detector modules.

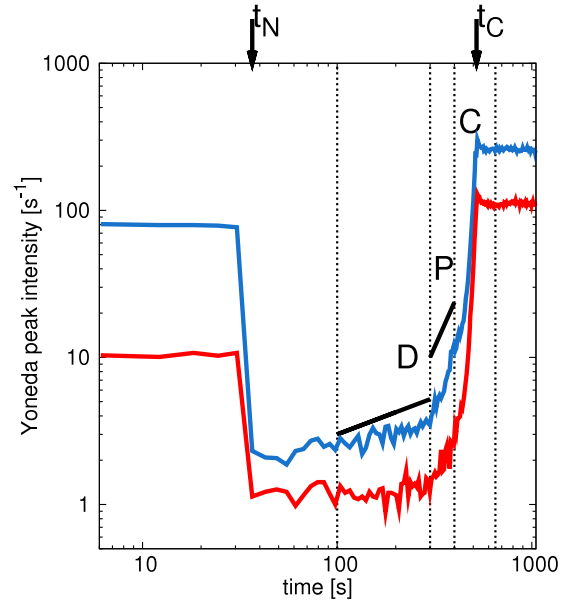


Figure 6. Evolution of Yoneda peak intensity of Au (red) and PS (blue) as a function of time. One can distinguish three regions. The solid lines represent power laws for the intensity $I \propto t^{0.5}$ in region AD and $I \propto t^3$ in region P. Region C shows the final evaporation of the solvent and compaction of the installed Au nanoparticle and PS layer due to evaporation of the residual water, resulting in decreased roughness of the layers. At t_N the droplet is deposited, at t_C the structures start compacting.

3. Experimental results

3.1. Kinetics of structure formation after droplet deposition

To obtain real-time information on the nanostructuring process caused by the deposition of the droplet of the Au nanoparticle solution on the pre-patterned substrate, we combined *in situ* imaging ellipsometry and μ GISAXS (see figure 3). Both give complementary information and thus yield insights in the complex kinetics. With μ GISAXS we address lateral structures and correlations along the surface normal in the nanoscale. Figure 5(a) shows the evolution of the intensity $I(q_y, t)_{\alpha_f = \alpha_c(\text{Si})}$ as a function of q_y and time t at constant exit angle $\alpha_f = \alpha_c(\text{Si})$. The corresponding map of the detector cut, $I(q_z, t)_{q_y=0}$, is shown in figure 5(b). The intensity is colour coded on a logarithmic scale. From the time-dependent changes of the intensity four different times are distinguishable (as marked in figure 5(a)):

- The droplet deposition time (N). The scattered intensity suddenly drops due to absorption of the x-ray beam by the Au nanoparticle solution.
- The rearrangement period (D). Two strong intensity side maxima, corresponding to the structure of the PS colloids on the Si surface, evolve. These maxima indicate a well defined nearest neighbour distance of the PS colloids. With increasing time the positions of the maxima shift slightly and finally the maxima disappear completely.
- The Au nanoparticle deposition (P). In this time region, strong scattered intensity around $q_y \approx 0.4 \text{ nm}^{-1}$ becomes

visible. This is due to the build-up of the Au nanoparticle layer on the pre-patterned and modified nanostructure.

- The compaction period (C). When the water finally evaporates, the rearranged and deposited structures become compact [35, 25].

After the compaction, a strong intensity increase is observed at the position of the Yoneda peak up to the position of the specular beam stop, when compared to the intensity prior to droplet deposition. This indicates an increased roughness of the PS layer as well as the deposition of the Au nanoparticles, as $\alpha_c(\text{Au}) = 0.328^\circ > \alpha_c(\text{PS}) = 0.096^\circ$.

In order to detail this, the temporal evolution of the intensity at the Yoneda peak positions of PS and Au, $I(q_y = 0, t)_{\alpha_f = \alpha_c(\text{Au,PS})}$, are displayed in figure 6. The droplet deposition is observed as a sudden and strong decrease in intensity at $t_N = 36.6 \text{ s}$. At $t_A = 94 \text{ s}$ after droplet deposition t_N , a first increase in the PS Yoneda peak intensity is visible. This intensity increase is followed by a $t^{0.5}$ power law, indicating the influence of diffusion of the PS colloids or larger domains [55]. This means, that inside the PS colloid layer the individual PS colloids become mobile and the layer rearranges. In detail, we observe segregation of the PS colloids and clustering of the gold in the interstices. This coincides well with the observation of the two side maxima in figure 5(a), period D. In region P, the Au Yoneda peak intensity also starts increasing. Both Yoneda peak intensities follow a t^3 law, indicating strong roughness changes. The model will be discussed below. Remarkably, the start of Au nanoparticle deposition kinetics is delayed with respect to the

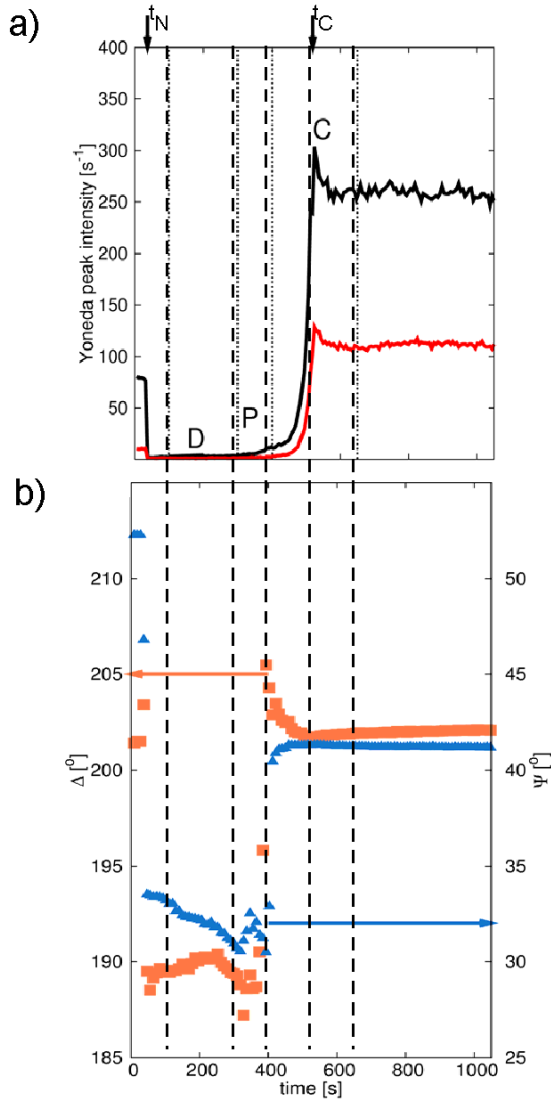


Figure 7. (a) Intensity evolution of the Yoneda peak intensity as a linear plot. (b) Evolution of Δ and Ψ during droplet evaporation. The five thick dashed lines indicate different stages from droplet deposition and subsequent drying. Clearly, the four curves coincide. In region P and C strong changes are visible owing to roughness changes of the PS layer and agglomeration of the Au particles. While the compaction of the PS and Au layer is clearly visible in (a), Δ and Ψ only change slightly in this time regime before levelling-off to their equilibrium value.

rearrangement kinetics of the PS layer. In the compaction period C the installed and rearranged layers become compact due to evaporation of the residual water. The roughness of the layers decreases, thus leading to a slight decrease of the intensity. One notes also that the final intensity is increased with respect to that at $t = 0$ s, due to the addition of Au nanoparticles and the overall increased roughness.

The solvent evaporation process is monitored *in situ* by imaging ellipsometry. The resulting Δ and Ψ are shown in combination with the evolution of the Yoneda peak intensity on a linear scale in figure 7. Again, the three different time regions can be distinguished, and coincide quite well as deduced from the two complementary methods. However, while the

Table 1. Results of the simulation at the indicated times. d denotes the mean diameter of the simulated structures, $R_{d,\min,\max}$ the cut-off limit of the distribution (i.e. $d_0 \pm R_d$), $\Delta d_0/d_0$ the width of the particle size distribution, ξ the simulated distance and $\Delta\xi$ its Gaussian smearing as full width half maximum.

Layer	time (s)	d_0 (nm)	$R_{d,\min}$ (nm)	$R_{d,\max}$ (nm)	$\Delta d_0/d_0$	ξ (nm)	$\Delta\xi$ (nm)
PS	0	90	80	100	0.1	90	20
PS	696	100	90	300	0.5	120	40
Au	696	20	13	26	0.1	30	10

compaction period is clearly visible in the μ GISAXS data, it is only visible as a slight change in the evolution of the imaging ellipsometry data. Thus imaging ellipsometry observes only three of the four different processes.

To quantify the nanostructuring, we refer to the two-dimensional (2D) μ GISAXS pattern in figure 8(a) and the corresponding out-of-plane cuts at $\alpha_f = \alpha_c(\text{Si})$ in figure 8(b) at $t = 0$ and 696 s (prior to and after deposition). The solid lines indicate simulations using the software package IsGISAXS [54]. We used a one-dimensional (1D) paracrystalline model for both the PS and Au layers with the details given in table 1. For $t = 0$ s, with just the pristine PS layer being present, well-pronounced side maxima are visible. This is confirmed by the AFM image in figure 2(a). After drying, the structures are smeared out. In particular an intensity increase around $q_y \approx 0.4 \text{ nm}^{-1}$ is clearly visible as a shoulder in the cuts (see figure 8(b)). This shoulder indicates agglomerations of Au nanoparticles (see figure 2(c)). Furthermore, the rearrangement and resulting increase of roughness in the PS layer is corroborated by the AFM image in figure 2(b). The IsGISAXS simulations also display a shift of the particle size distribution from a well defined diameter of $d(\text{PS}) = 45 \text{ nm}$ to a broad distribution with particle diameters up to 300 nm. These large values indicate also agglomerations of PS colloids, resulting in an increased roughness after solvent evaporation. Additionally their mean distance and distance distribution increase. Both observations correspond well with the AFM results. We find an increased domain size after the rearrangement of the PS colloids.

3.2. Static investigation of the installed morphology

Prior to and after droplet deposition (dried state), the region of the dried droplet was scanned with μ GISAXS (see figure 1) using a step size of $100 \mu\text{m}$. The PS layer as well as the channel were investigated. In figures 9(a) and (b) we present the maps of the out-of-plane cuts prior to droplet deposition and after drying of the droplet, respectively. Clearly, the edge of the channel is visible (1) as well as the rim of the dried droplet (2). A strong intensity enhancement is visible around $q_y \approx 0.4 \text{ nm}^{-1}$ in the droplet regions due to the deposition and agglomeration of the Au nanoparticles in this area. This confirms the deposition of gold nanoparticles inside the dried droplet area.

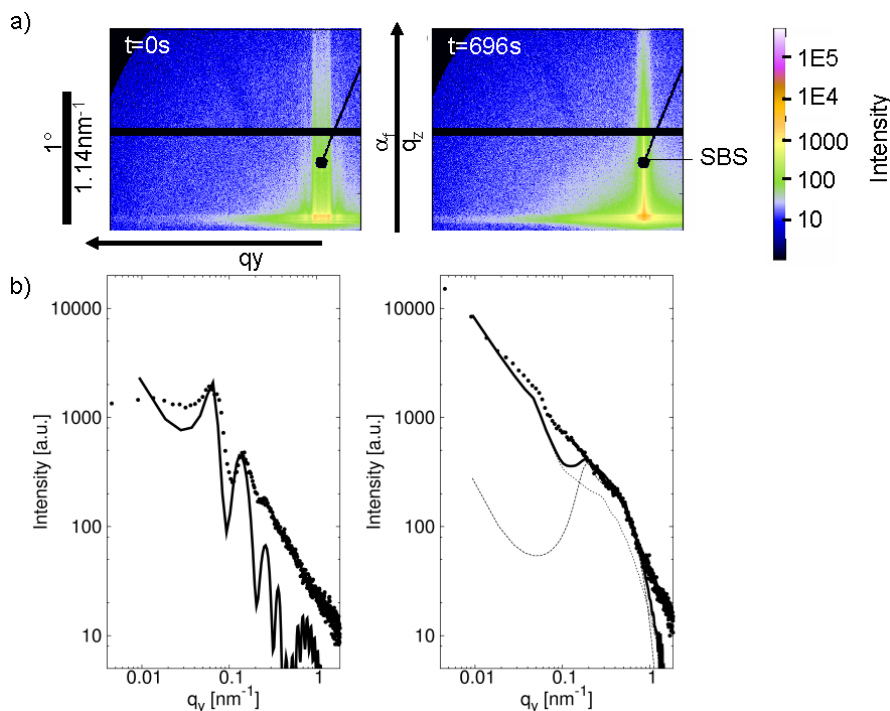


Figure 8. (a) Two-dimensional (2D) μ GISAXS pattern obtained prior to ($t = 0$ s) and at $t = 696$ s after the Au colloidal droplet deposition. Clearly visible is the separation between the different modules of the detector as well as the specular beam stop. (b) Out-of-plane cuts performed at $\alpha_c(\text{Si}) = 0.141^\circ$ at $t = 0$ and 696 s. The thick solid line denotes the simulation using IsGISAXS. For $t = 696$ s, the scattered intensity consists of two contributions, namely Au nanoparticle agglomerates in the region $q_y \approx 0.3 \text{ nm}^{-1}$ and PS spheres in the region $q_y \approx 0.04 \text{ nm}^{-1}$, represented by the thin solid lines.

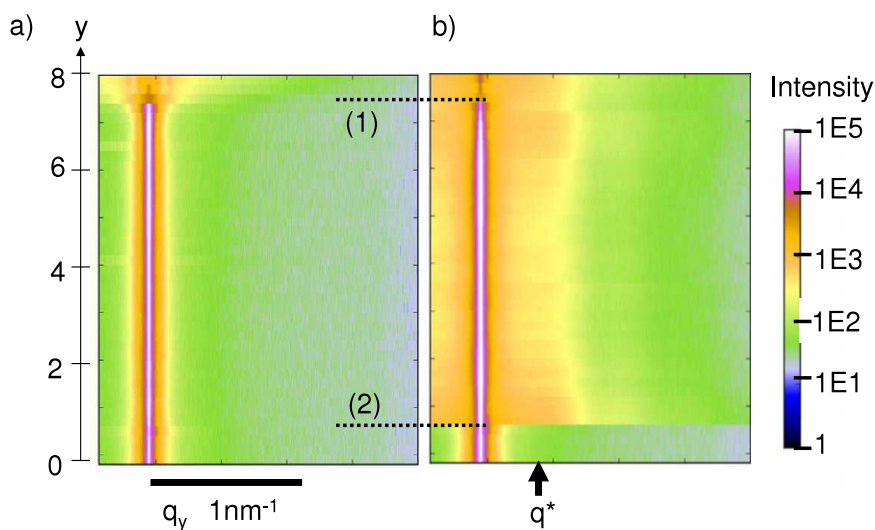


Figure 9. Map of the out-of-plane cuts of the scanned region indicated in figure 1. Clearly visible is the edge of the channel (1) as well as the outer rim of the droplet (2): (a) prior to deposition, (b) after drying of the droplet. The scale bar is indicated.

3.3. Model of structure formation

The results from imaging ellipsometry and μ GISAXS suggest the following model for the nanostructuring during solution casting of a Au colloidal droplet on top of a pre-patterned PS colloidal layer. The model consists of four different time regimes, as sketched in figure 10. After spin-coating, in its pristine state, the pre-patterned substrate consists of a PS colloidal layer with a perturbed hexagonal arrangement

(see also figure 2(a)). After deposition of the droplet containing an aqueous solution of Au colloids, the PS particles rearrange into larger domains (see the sketch in figures 10(b) and (c)). This is indicated by the shift in the particle size distribution (see table 1). Its temporal behaviour follows a $t^{0.5}$ law, corroborating diffusive rearrangement processes (see figure 6). The build-up of the Au colloidal particle layers starts with a distinct time delay, when the power law for the PS

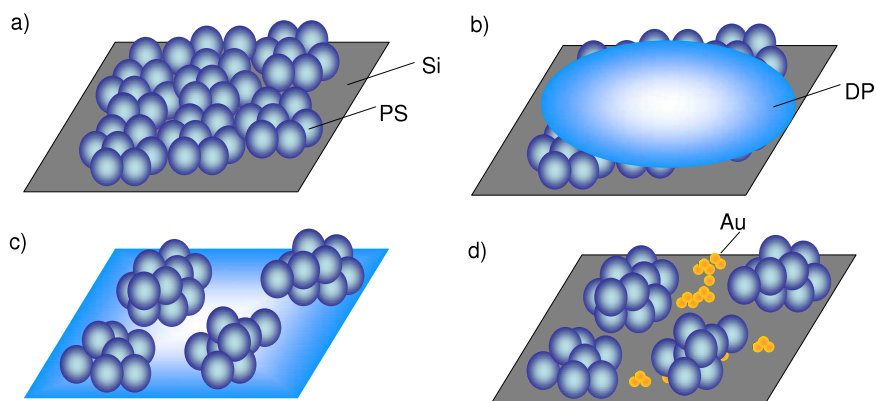


Figure 10. Model for structure formation during solution droplet casting of a Au colloidal solution onto a PS layer. (a) Sketch of the PS layer. (b) Droplet deposition. (c) Rearrangement phase of the PS layer while the droplet is drying (D in figure 6). (d) Au colloid deposition phase with subsequent compaction of the installed structures (P and C in figure 6).

rearrangement changes to t^3 . In the final state (see figure 10(d)) larger PS structures as well as agglomerated Au nanoparticles are present. This agrees very well with the AFM images in figures 2(b) and (c). It becomes clear that the layers show an increased roughness compared to the pristine PS colloidal layer. This roughness increase is also confirmed by the Δ and Ψ maps of the imaging ellipsometry in figures 1(b) and (c).

4. Summary

We have presented an investigation of the cluster formation of Au nanoparticles on top of a pre-structured PS colloidal thin film. During Au cluster formation, the PS colloidal thin film segregates. This can be explained if the interaction between gold and substrate and polymer and substrate is stronger than that between the two types of nanoparticles which in turn leads to segregation. Observing the nanostructuring process of this bimodal system in real time, we are able to identify different time regimes and length scales which can be connected to the build-up of a Au nanoparticle layer and a morphological rearrangement of the PS layer. We used the novel combination of *in situ* microbeam grazing incidence small-angle x-ray scattering experiment and imaging ellipsometry at the MiNaXS beamline of PETRA III, DESY. Our results indicate a separated structure of Au nanoparticle agglomerations and a clustering of PS colloids into larger domains. Thereby, new structural alloys in the field of metal-polymer nanocomposites made by solution casting can be envisaged.

Acknowledgments

The authors thank the Bundesministerium für Bildung und Forschung for financial support (grant 05KS7W01). Portions of this research were carried out at the light source PETRA III at HASYLAB/DESY. DESY is a member of the Helmholtz Association (HGF).

References

- [1] Faupel F, Zaporjtchenko V, Strunskus T and Elbahri M 2010 *Adv. Eng. Mater.* **12** 1177
- [2] Renaud G *et al* 2003 *Science* **300** 1416
- [3] Abul Kashem M M *et al* 2009 *Macromolecules* **42** 6202
- [4] Lin Y *et al* 2005 *Nature* **434** 55
- [5] Siffalovic P, Majkova E, Chitu L, Jergel M, Luby S, Capek I, Satka A, Timmann A and Roth S V 2008 *Small* **4** 2222
- [6] Bauer G, Hassmann J, Walter H, Haglmüller J, Mayer C and Schalkhammer T 2003 *Nanotechnology* **14** 1289
- [7] Walter H, Bauer G, Domnick R, Jakopic G and Leitner A 2006 *Opt. Eng.* **45** 103801
- [8] Pakula C, Zaporjtchenko V, Strunskus T, Zargarani D, Herges R and Faupel F 2010 *Nanotechnology* **21** 465201
- [9] Zaporjtchenko V, Strunskus T, Erichsen J and Faupel F 2001 *Macromolecules* **34** 1125
- [10] Kaune G, Ruderer M A, Metwalli E, Wang W, Couet S, Schlage K, Röhlberger R, Roth S V and Müller-Buschbaum P 2009 *ACS Appl. Mater. Interfaces* **1** 353
- [11] Sciancalepore C, Cassano T, Curri M L, Mecerreyes D, Valentini A, Agostiano A, Tommasi R and Striccoli M 2008 *Nanotechnology* **19** 205705
- [12] Abargues R, Marques-Hueso J, Canet-Ferrer J, Pedrueza E, Valdes J L, Jimenez E and Martynez-Pastor J P 2008 *Nanotechnology* **19** 355308
- [13] Takele H, Greve H, Pochstein C, Zaporjtchenko V and Faupel F 2006 *Nanotechnology* **17** 3499
- [14] Xia Y, Gates B, Yin Y and Lu Y 2000 *Adv. Mater.* **12** 693
- [15] Lee T J *et al* 2009 *Nanotechnology* **20** 135204
- [16] Kim D M, Park S, Lee T J, Hahm S G, Kim K, Kim J C, Kwon W-S and Ree M 2009 *Langmuir* **25** 11713
- [17] Zaporjtchenko V, Strunskus T, Behnke K, Von Bechtolsheim C, Kiene M and Faupel F 2000 *J. Adhes. Sci. Technol.* **14** 467
- [18] Tognalli N G, Scodeller P, Flexer V, Szamocki R, Ricci A, Tagliacucchi M, Calvo E J and Fainstein A 2009 *Phys. Chem. Chem. Phys.* **11** 7412–23
- [19] Yu X, Zhou S, Zheng X, Guo T, Xiao Y and Song B 2009 *Nanotechnology* **20** 235702
- [20] Calvo E J, Rothacher M S, Bonazzola C, Wheeldon I R, Salvarezza R C, Vela M E and Benitez G 2005 *Langmuir* **21** 7907–11
- [21] Shah S A, Nag M, Kalagara T, Singh S and Manorama S V 2008 *Chem. Mater.* **20** 2455–60
- [22] Kim D, Jeong S, Park B K and Moona J 2006 *Appl. Phys. Lett.* **89** 264101

- [23] Gebhardt R, Burghammer M, Riekel C, Roth S V and Müller-Buschbaum P 2008 *Macromol. Biosci.* **8** 347
- [24] Kuhlmann M, Feldkamp J M, Patommel J, Roth S V, Timmann A, Gehrke R, Müller-Buschbaum P and Schroer C G 2009 *Langmuir* **25** 7241
- [25] Roth S V, Autenrieth T, Grübel G, Riekel C, Burghammer M, Hengstler R, Schulz L and Müller-Buschbaum P 2007 *Appl. Phys. Lett.* **91** 091915
- [26] Lechmann M C, Kessler D and Gutmann J S 2009 *Langmuir* **25** 10202
- [27] Gebhardt R, Vendrely C, Burghammer M and Riekel C 2009 *Langmuir* **25** 6307
- [28] Lecomte S, Matejka P and Baron M H 1998 *Langmuir* **14** 4373
- [29] Sarangi S N, Goswami K and Sahu S N 2007 *Biosens. Bioelectron.* **22** 3086
- [30] Strick T R, Allemand J-F, Bensimon D, Bensimon A and Croquette V 1996 *Science* **271** 1835
- [31] Wolkenhauer M, Bumbu G-G, Cheng Y, Roth S V and Gutmann J S 2006 *Appl. Phys. Lett.* **89** 054101
- [32] Kaune G, Memesa M, Meier R, Ruderer M A, Diethert A, Roth S V, D'Acunzi M, Gutmann J S and Müller-Buschbaum P 2009 *ACS Appl. Mater. Interfaces* **1** 2862
- [33] Haw M D, Gillie M and Poon W C K 2002 *Langmuir* **18** 1626
- [34] Müller-Buschbaum P, Bauer E, Pfister S, Roth S V, Burghammer M, Riekel C, David C and Thiele U 2006 *Europhys. Lett.* **73** 35
- [35] Siffalovic P, Majkova E, Chitu L, Jergel M, Luby S, Satka A and Roth S V 2007 *Phys. Rev. B* **76** 195432
- [36] Gonuguntla M and Sharma A 2004 *Langmuir* **20** 3456
- [37] Poulard C and Damman P 2007 *Europhys. Lett.* **80** 64001
- [38] Nguyen V X and Stebe K J 2002 *Phys. Rev. Lett.* **88** 164501
- [39] Deegan R D 2000 *Phys. Rev. E* **61** 475
- [40] Denkov N D, Velev O D, Kralchevsky P A, Ivanov I B, Yoshimura H and Nagayama K 1993 *Nature* **361** 26
- [41] Roth S V, Müller-Buschbaum P, Timmann A, Perlich J and Gehrke R 2007 *J. Appl. Crystallogr.* **40** 346
- [42] Roth S V, Rothkirch A, Autenrieth T, Gehrke R, Wroblewski T, Burghammer M C, Riekel C, Schulz L, Hengstler R and Müller-Buschbaum P 2010 *Langmuir* **26** 1496
- [43] Roth S V, Kuhlmann M, Walter H, Snigirev A, Snigireva I, Lengeler B, Schroer C, Burghammer M, Riekel C and Müller-Buschbaum P 2009 *J. Phys.: Condens. Matter* **21** 264012
- [44] Körstgens V, Wiedersich J, Meier R, Perlich J, Roth S V, Gehrke R and Müller-Buschbaum P 2010 *Anal. Bioanal. Chem.* **396** 139
- [45] Schmaljohann D, Nitschke M, Schulze R, Eing A, Werner C and Eichhorn K-J 2005 *Langmuir* **21** 2317
- [46] Roth S V, Burghammer M, Riekel C, Müller-Buschbaum P, Diethert A, Panagiotou P and Walter H 2003 *Appl. Phys. Lett.* **82** 1935
- [47] Roth S V *et al* 2006 *Appl. Phys. Lett.* **88** 021910
- [48] Roth S V, Döhrmann R, Dommach M, Kuhlmann M, Kröger I, Gehrke R, Walter H, Schroer C, Lengeler B and Müller-Buschbaum P 2006 *Rev. Sci. Instrum.* **77** 085106
- [49] Müller-Buschbaum P 2009 A basic introduction to grazing incidence small angle x-ray scattering *Applications of Synchrotron Light to Noncrystalline Diffraction in Materials and Life Sciences (Springer Lecture notes in Physics vol 776)* ed T A Ezquerra, M Garcia-Gutierrez, A Nogales and M Gomez (Berlin: Springer) pp 61–90
- [50] Fratzl P 2003 *J. Appl. Crystallogr.* **36** 397
- [51] Yoneda Y 1963 *Phys. Rev.* **131** 2010
- [52] Lengeler B, Schroer C G, Kuhlmann M, Benner B, Günzler T F, Kurapova O, Zontone F, Snigirev A and Snigireva I 2005 *J. Phys. D: Appl. Phys.* **38** A218
- [53] Directly Programmable Data Analysis Kit <http://www.desy.de/~benecke/dpdak>
- [54] Lazzari R 2002 *J. Appl. Crystallogr.* **35** 406
- [55] Martin-Gassin G, El Harfouch Y, Benichou E, Bachelier G, Russier-Antoine I, Jonin C, Roux S, Tillement O and Brevet P-F 2008 *J. Phys.: Condens. Matter* **20** 055228